Majorana neutrino mass constraints in the landscape of nuclear matrix elements

Eligio Lisi[1] and Antonio Marrone[2,1]

[1]*Istituto Nazionale di Fisica Nucleare, Sezione di Bari, Via Orabona 4, 70126 Bari, Italy*
[2]*Dipartimento Interateneo di Fisica "Michelangelo Merlin", Via Amendola 173, 70126 Bari, Italy*

(Received 23 April 2022; accepted 15 July 2022; published 27 July 2022)

We discuss up-to-date constraints on the Majorana neutrino mass $m_{\beta\beta}$ from neutrinoless double beta decay ($0\nu\beta\beta$) searches in experiments using different isotopes: KamLAND-Zen and EXO (^{136}Xe), GERDA and MAJORANA (^{76}Ge) and CUORE (^{130}Te). Best fits and upper bounds on $m_{\beta\beta}$ are explored in the general landscape of nuclear matrix elements (NME), as well as for specific NME values obtained in representative nuclear models. By approximating the likelihood of $0\nu\beta\beta$ signals through quadratic forms, the analysis of separate and combined isotope data becomes exceedingly simple, and allows us to clarify various aspects of multi-isotope data combinations. In particular, we analyze the relative impact of different data in setting upper bounds on $m_{\beta\beta}$, as well as the conditions leading to nonzero $m_{\beta\beta}$ at best fit, for variable values of the NMEs. Detailed results on $m_{\beta\beta}$ from various combinations of data are reported in graphical and numerical form. Implications for future $0\nu\beta\beta$ data analyses and NME calculations are briefly discussed.

DOI: 10.1103/PhysRevD.106.013009

I. INTRODUCTION

The process of neutrinoless double beta decay ($0\nu\beta\beta$),

$$(Z, A) \to (Z + 2, A) + 2e^-, \tag{1}$$

expected to occur for some candidate isotopes (Z, A) if neutrinos are Majorana fermions, may be interpreted as a miniature event of leptonic matter creation or "little bang," whose discovery would have profound implications for particle and nuclear physics and for cosmology [1].

In the standard three-neutrino paradigm [2], the process would be mediated by three Majorana neutrino mass states ν_i ($i = 1, 2, 3$) mixed with the three known flavor states ν_α ($\alpha = e, \mu, \tau$) via a unitary mixing matrix $U_{\alpha i}$, parametrized in terms of three mixing angles $(\theta_{12}\theta_{13}, \theta_{23})$, one (Dirac) phase δ, and two (Majorana) phases $\varphi_{1,2}$. The relevant particle physics parameter is the effective Majorana neutrino mass $m_{\beta\beta}$, defined as

$$m_{\beta\beta} = |U_{e1}^2 m_1 + U_{e2}^2 m_2 + U_{e3}^2 m_3|, \tag{2}$$

and related to the observable $0\nu\beta\beta$ decay half-life T_i in each isotope $i = (Z, A)$ via

$$\frac{1}{T_i} = G_i M_i^2 m_{\beta\beta}^2, \tag{3}$$

where G_i is the phase space, and M_i is the nuclear matrix element (NME) for the decay.

It is useful to contrast the Majorana ν mass $m_{\beta\beta}$ with the sum of neutrino masses

$$\Sigma = m_1 + m_2 + m_3, \tag{4}$$

that, being a source of gravity, can produce observable cosmological effects [2]. Figure 1 shows the regions allowed in the $(\Sigma, m_{\beta\beta})$ plane at the 2σ level ($\Delta\chi^2 = 4$) by a global analysis of neutrino oscillation data [3], for masses m_i either in normal ordering (NO, $m_{1,2} < m_3$) or in inverted ordering (IO, $m_3 < m_{1,2}$). For a given value of Σ, the vertical spread of $m_{\beta\beta}$ is mostly due to the unknown relative phases of the U_{ei} matrix elements in Eq. (2).

Current cosmological data provide typical upper bounds on Σ at the level of $O(100)$ meV, that are more easily accommodated in NO than in IO [3]; see also the overview of recent constraints on Σ and their impact on ν mass ordering in [4]. Several $0\nu\beta\beta$ decay searches are also exploring the O(100) meV range for $m_{\beta\beta}$ [1,2]; in particular, the latest constraints from KamLAND-Zen [5] (^{136}Xe) can plunge into the region $m_{\beta\beta} \sim$ few $\times$ 10 meV for

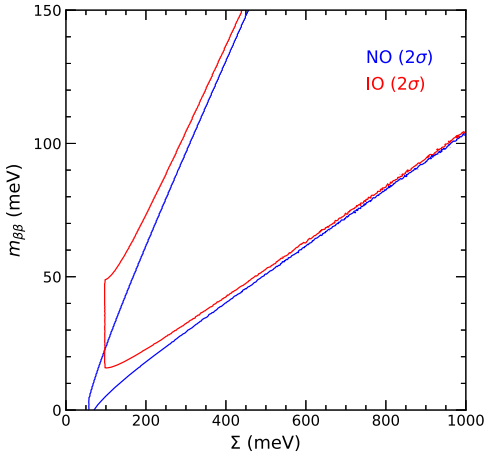

FIG. 1. Majorana ν mass $m_{\beta\beta}$ versus the sum of ν masses Σ (both in units of 10^{-3} eV). The points inside the blue (NO) and red (IO) wedge-shaped regions are allowed at 2σ by the global analysis of ν oscillation data. Adapted from [3].

favorable values of the NME.[1] Other very sensitive $0\nu\beta\beta$ searches, all probing half-lives $T_i > 10^{25}$ y at 90% C.L., have been performed by the experiments EXO [6] (^{136}Xe), GERDA [7] and MAJORANA [8] (^{76}Ge), and CUORE [9] (^{130}Te).

Building upon previous work [3], we discuss in detail how to combine current (Xe, Ge, Te) data for given NME values.[2] The approach allows a do-it-yourself $0\nu\beta\beta$ global analysis in terms of χ^2 functions with (up to) quadratic dependence on the signal strength $1/T_i$, which is a good approximation to recent results [3,10,11]. In particular, we describe how to derive $m_{\beta\beta}$ constraints at a given confidence level, using both separate and combined (Xe, Ge, Te) data, for generic values of the nuclear matrix elements (the "NME landscape"), as well as for representative NME values from different nuclear models. Our approach clarifies interesting aspects of the $0\nu\beta\beta$ data analysis, such as the relative importance of each isotope in determining (non) zero best fits and upper bounds for $m_{\beta\beta}$.

The paper is structured as follows: In Sec. II we describe the ingredients of our analysis in terms of notation, parametrization of experimental results for (Xe, Ge, Te), and associated NME's. In Sec. III we discuss the main results of the analysis in terms of $m_{\beta\beta}$ constraints, by considering two qualitatively different situations: (1) cases where, *a priori*, $m_{\beta\beta} = 0$ is preferred, and (2) more general cases where the best fit may be at $m_{\beta\beta} > 0$. Upper bounds on $m_{\beta\beta}$ are explored both graphically and numerically in the NME landscape, by using separate and combined (Xe, Ge, Te) data. In Sec. IV we summarize our results and comment on further applications and perspectives.

II. INGREDIENTS OF THE ANALYSIS

In this section we introduce the notation, the experimental results and their parametrization, the landscape of NME and the phase space related to the three isotopes Xe, Ge and Te.

A. Notation and units

Following [3], we introduce the inverse half-life

$$S_i = 1/T_i, \tag{5}$$

that represents, up to a constant factor, the observable decay rate or signal strength in each $i = (Z, A)$ isotope. Equation (3) reads then

$$S_i = G_i M_i^2 m_{\beta\beta}^2. \tag{6}$$

To keep the notation compact, we absorb in G_i terms as $1/m_e^2$ and g_A^4 (where $g_A = 1.276$ [12] is the bare value of the axial-vector coupling), that are factorized out in other conventions. In particular, we can make contact with the notation of [1], where $1/T = G_{01} g_A^4 M_{0\nu}^2 m_{\beta\beta}^2/m_e^2$, by identifying $G = G_{01} g_A^4/m_e^2$ and $M = M_{0\nu}$ for each isotope i. We also follow [1] by taking the M_i as positive real numbers, referred to the bare value of g_A (unless otherwise noticed). Qualitative effects of the so-called quenching of g_A in nuclear matter [13] are separately commented below.

Finally, the following units are adopted:

$$[m_{\beta\beta}] = \text{meV}, \tag{7}$$

$$[T_i] = 10^{26} y, \tag{8}$$

$$[S_i] = 10^{-26} y^{-1}, \tag{9}$$

$$[G_i] = 10^{-26} y^{-1}\ (\text{meV})^{-2}. \tag{10}$$

B. Experimental inputs and parametrizations

In principle, the $0\nu\beta\beta$ data analysis would be straightforward, if likelihood profiles were provided for the signal strength S_i (or for T_i) in each experiment, e.g., in terms of a function $\chi_i^2(S_i)$. Barring error correlations among independent experiments, one should sum up the χ_i^2 functions,

[1]The range $m_{\beta\beta} \simeq 16$–49 meV, spanning the leftmost edge of the IO region in Fig. 1, is often (but improperly) dubbed in $0\nu\beta\beta$ jargon as "IO region," despite being compatible with both IO and NO (as well as the quasidegenerate region at higher $m_{\beta\beta}$). The misnomer may originate from plots of $m_{\beta\beta}$ versus the lightest ν mass m_l, where two elongated stripes for IO and NO appear in log scale as $m_l \to 0$, see e.g., [1,5]. However, the asymptotic separation of such stripes has no physical relevance, since m_l is not directly measurable and cannot be resolved with an accuracy better than an observable such as Σ. Projecting away m_l (as in Fig. 1) makes the point clear.

[2]For simplicity, we shall generally drop superscripts for the Xe, Ge, and Te isotopes.

express the S_i in terms of $m_{\beta\beta}$ via Eq. (6) for a given set of M_i, and map the resulting best fits and allowed regions for $m_{\beta\beta}$. In practice, experimental papers often focus on a single point of the likelihood profile (e.g., the T_i bound at 90% C.L.), whereas its shape has to be derived from supplementary information.

A useful empirical fact, first noted in [10] and further elaborated in [3], is that the functions $\chi_i^2(S_i)$ are often well approximated by (up to) quadratic forms in S_i; see also the recent results in [11]. Such forms cover $0\nu\beta\beta$ decay searches ranging from zero background (with Poissonian, linear dependence on S_i) to large backgrounds (with Gaussian, quadratic dependence on S_i) [3]. In particular, we have checked that the quadratic approximation works very well also for the latest KamLAND-Zen data [5,14], up to 3σ level at least.

Each experimental result is thus parametrized through a function $\Delta\chi_i^2(S_i)$ of the form:

$$\Delta\chi_i^2(S_i) = a_i S_i^2 + b_i S_i + c_i, \tag{11}$$

where the offset c_i is set by the condition that the minimum value $\Delta\chi_i^2 = 0$ is reached within the physical region $S_i \geq 0$, namely,

$$c_i = \begin{cases} 0 & \text{for } b_i \geq 0, \\ b_i^2/4a_i & \text{for } b_i < 0. \end{cases} \tag{12}$$

For $a_i > 0$ the $\Delta\chi_i^2$ functions are parabolic, with a vertex placed at either $S_i = 0$ (null result, $b_i = 0$), or $S_i < 0$ (negative fluctuation in the unphysical region, $b_i > 0$), or $S_i > 0$ (physical signal or positive fluctuation, $b_i < 0$). In the latter case, the offset c_i guarantees $\Delta\chi_i^2 = 0$ at $S_i = -b_i/2a_i$. For $a_i = 0$, the $\Delta\chi_i^2$ functions are linear. For the same isotope, the results of independent experiments are combined by summing their $\Delta\chi_i^2$'s, and readjusting the total offset as per Eq. (12). In all cases, 90% C.L. bounds on the half-life ($T_{90} = 1/S_{90}$) are obtained by imposing $\Delta\chi_i^2(S_{90}) = 2.706$.

Table I, updated from [3] with the inclusion of the latest KamLAND-Zen results [5], reports the coefficients of the parametrization in Eq. (11) and the T_{90} bounds for the most sensitive current experiments ($T_{90} > 0.1$), as well as for combinations of experiments using the same isotope. For later purposes, we also consider hypothetical CUORE results for an exactly null signal, denoted as CUORE* (or Te*).

Figure 2 shows the numerical information of Table I in graphical form; the left and right panels refer, respectively, to separate experiments and to same-isotope combinations (Xe, Ge, Te). A few remarks about these graphs and the numerics are in order. The case of linear $\Delta\chi^2$ functions applies to current GERDA and MAJORANA results, whose combination (denoted as Ge) sets a bound $T_{90} = 2.07$ stronger than for GERDA alone ($T_{90} = 1.8$). All the other experiments are characterized by parabolic functions. KamLAND-Zen and EXO report, respectively, a negative and a positive fluctuation, that partly cancel in their combination (denoted as Xe). As a result, the Xe bound $T_{90} = 2.26$ is slightly weaker ($T_{90} = 2.26$) than for KamLAND-Zen alone ($T_{90} = 2.3$). Note that, for both the Ge and Xe combinations, it is $\Delta\chi_i^2 = 0$ at $S_i = 0$.

Results for the Te isotope depend on the single CUORE experiment, which shows a positive fluctuation at the level of $0.64\sigma = [\Delta\chi_i^2(0)]^{1/2}$. As anticipated we consider, besides the real Te results, also hypothetical Te* results, where this fluctuation is canceled by setting $b_i = 0$ (and thus also $c_i = 0$). The half-time limit for Te* ($T_{90} = 0.301$) is in reasonable agreement with the median sensitivity quoted by the CUORE experiment for null result ($T_{90} = 0.28$). In Sec. III, the combination of Xe, Ge, and Te* results (all with $\Delta\chi_i^2 = 0$ at $S_i = 0$) will provide

TABLE I. Coefficients of the quadratic parametrization of $\Delta\chi_i^2$ in terms of the signal strength $S_i = 1/T_i$. The first two columns report the isotope and the names of the experiments or their combination. The next three columns report our evaluation of the coefficients (a_i, b_i, c_i) for the various experiments (upper five rows) and for their combinations in the same isotope (lower rows). The bottom row refers to the case of CUORE sensitivity for null result (tagged by *). The sixth column reports our 90% C.L. ($\Delta\chi^2 = 2.706$) half-life limits T_{90}, to be compared with the experimentally quoted one in the seventh column (as taken from the reference in the eighth column, when applicable).

Isotope	Experiment or combination	a_i	b_i	c_i	$T_{90}/10^{26}$ y	T_{90} (expt.)	Reference
^{136}Xe	KamLAND-Zen	5.157	3.978	0.000	2.300	2.3	[5]
^{136}Xe	EXO	0.440	−0.338	0.065	0.350	0.35	[6]
^{76}Ge	GERDA	0.000	4.867	0.000	1.800	1.8	[7]
^{76}Ge	MAJORANA	0.000	0.731	0.000	0.270	0.27	[8]
^{130}Te	CUORE	0.245	−0.637	0.414	0.216	0.22	[9]
^{136}Xe	Xe (KamLAND-Zen + EXO)	5.597	3.640	0.000	2.260	⋯	⋯
^{76}Ge	Ge (GERDA + MAJORANA)	0.000	5.598	0.000	2.070	⋯	⋯
^{130}Te	Te (CUORE data as above)	0.245	−0.637	0.414	0.216	0.22	[9]
^{130}Te	Te* (CUORE*, sensitivity)	0.245	0.000	0.000	0.301	0.28	[9]

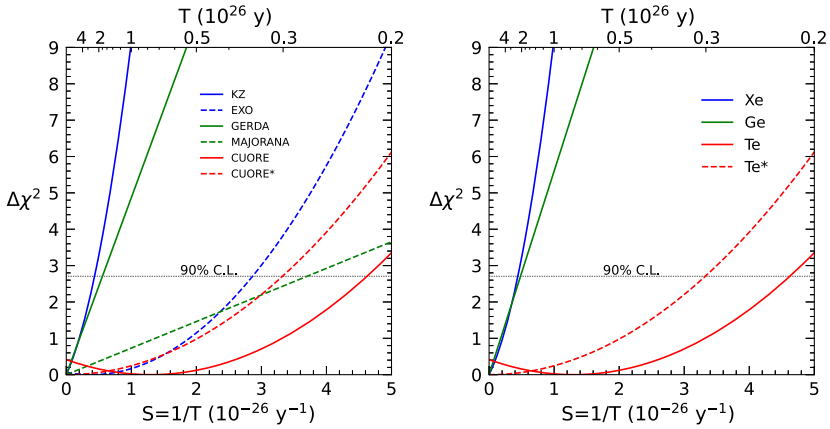

FIG. 2. $\Delta\chi^2$ functions in terms of the half-life T (top abscissa) and of the signal strength $S = 1/T$ (bottom abscissa). Left and right panels: separate experiments and their combinations for the same isotope, respectively. Dotted horizontal lines intersect the curves at 90% C.L. See the text for details.

a simple starting point, before discussing the full combination of Xe, Ge and Te constraints on $m_{\beta\beta}$.

C. Landscape of nuclear matrix elements

In order to study the combination of $0\nu\beta\beta$ results in full generality, we consider unconstrained values of the nuclear matrix elements $M_{\rm Xe}$, $M_{\rm Ge}$, $M_{\rm Te}$ in the numerical range $M_i \in [0.2, 20]$. Within this landscape, we also consider representative M_i values from four different approaches to nuclear modeling, including the nuclear shell model (SM), the quasiparticle random phase approximation (QRPA), the energy-density functional theory (EDF), and the interacting boson model (IBM). The NME values are taken from a recent compilation of results [15–26] as reported in [1] for the bare value of g_A (see Table I therein), and are listed in Table II for the sake of completeness.

TABLE II. Representative nuclear matrix elements $(M_{\rm Xe}, M_{\rm Ge}, M_{\rm Te})$ computed within four different models (SM, QRPA, EDF, and IMB) for bare value of g_A. Adapted from [1].

	$M_{\rm Xe}$	$M_{\rm Ge}$	$M_{\rm Te}$	Reference	Model
1	2.28	2.89	2.76	[15]	
2	2.45	3.07	2.96	[15]	
3	1.63	3.37	1.79	[16]	SM
4	1.76	3.57	1.93	[16]	
5	2.39	2.66	3.16	[17]	
6	1.55	5.09	1.37	[18]	
7	2.91	5.26	4.00	[19]	
8	2.72	4.85	4.67	[20]	QRPA
9	1.11	3.12	2.90	[21]	
10	1.18	3.40	3.22	[21]	
11	4.20	4.60	5.13	[22]	
12	4.77	5.55	6.41	[23]	EDF
13	4.24	6.04	4.89	[24]	
14	3.25	5.14	3.96	[25]	
15	3.40	6.34	4.15	[26]	IBM

Figure 3 shows the NME landscape in each of the three planes charted by pairs (M_i, M_j), together with the representative M_i values reported in Table II, which refer to the bare g_A. The issue of the effective g_A value to be used in nuclear matter, either bare or quenched by a factor q ($g_A \to q g_A$ with $q < 1$), is largely debated and model-dependent [1,13]. For NMEs dominated by the axial-vector (Gamow-Teller) component (as it is often the case), the

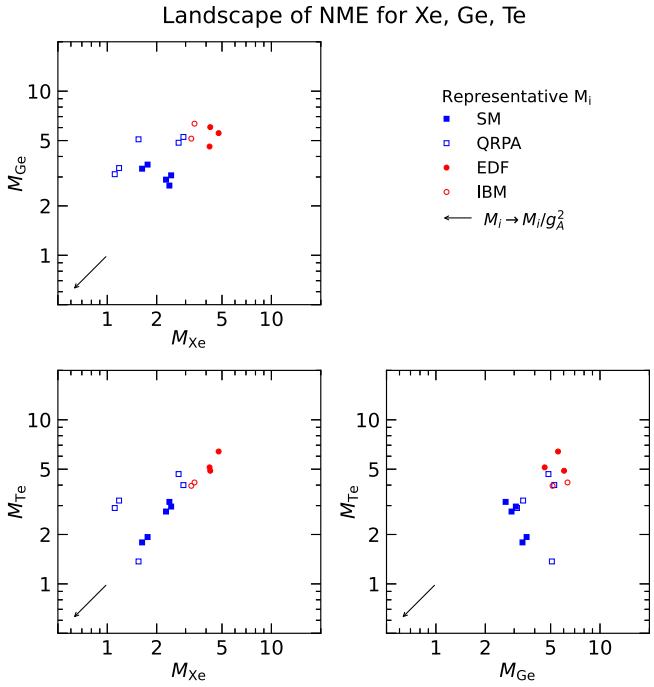

FIG. 3. Landscape of nuclear matrix elements $M_i = (M_{\rm Xe}, M_{\rm Ge}, M_{\rm Te})$, in each of the three planes charted by pairs (M_i, M_j). Also shown are the representative M_i values reported in Table II from different models (SM, QRPA, EDF, IBM). The arrows show the effect of rescaling each M_i as M_i/g_A^2 (representing typical quenching effects). See the text for details.

leading quenching effect would amount to rescaling the product $G_i M_i^2$ by a factor $q^4 \sim g_A^4$, that can be assumed to operate on M_i only ($M_i \to q^2 M_i$) if G_i is kept constant.

As a representative quenching effect one may consider, e.g., the typical case $qg_A \simeq 1$, namely, $q \sim 1/g_A$, leading to an approximate rescaling $M_i \to M_i/g_A^2$, as shown in each panel of Fig. 3 by an arrow (applicable to any marked point). Stronger quenching would be associated to longer arrows (not shown). On the other hand, quenching effects would be weaker for sizeable NME vector (Fermi) components, not scaling with q^2. Moreover, some M_i calculations may exhibit a milder dependence on qg_A for different reasons. In some QRPA calculations, e.g., $2\nu\beta\beta$ data are used to adjust the particle-particle parameter g_{pp}, partly trading the effect of quenching g_A from its bare value to unity [27]. In the same approach, large statistical covariances are observed among the M_i values for different isotopes, inducing noticeable effects on $m_{\beta\beta}$ constraints [27], as recently discussed in [3]. The marked points in Fig. 3 also seem to suggest an overall positive correlation (possibly enhanced by quenching effects) but, since they do not represent a statistical distribution, their covariances (if any) will be ignored.

Summarizing, the NME landscape in Fig. 3 is meant to cover a wide and continuous range of M_i values, either unquenched or arbitrarily quenched. Graphical results will be shown for unconstrained M_i values in this landscape. Marked points in Fig. 3 are meant to represent typical unquenched M_i (central values) as taken from the literature (see Table II), while the arrows provide visual guidance for typical quenching effects ($qg_A \sim 1$).

D. Phase space

The last ingredient is represented by the phase space G_i for $0\nu\beta\beta$ decay in $i =$ Xe, Ge and Te, that we take from the calculation in [26]. In our notation and units:

$$G_{\mathrm{Xe}} = 14.78 \times 10^{-6}, \tag{13}$$

$$G_{\mathrm{Ge}} = 2.40 \times 10^{-6}, \tag{14}$$

$$G_{\mathrm{Te}} = 14.42 \times 10^{-6}. \tag{15}$$

The phase space uncertainties [28] are much smaller than those related to $0\nu\beta\beta$ data and are not considered herein.

III. CONSTRAINTS ON THE MAJORANA NEUTRINO MASS

The previously discussed functions $\Delta\chi_i^2(S_i)$ can be recast in terms of quadratic functions of $m_{\beta\beta}^2$ through Eq. (6):

$$\Delta\chi_i^2 = \alpha_i m_{\beta\beta}^4 + \beta_i m_{\beta\beta}^2 + \gamma_i, \tag{16}$$

where the offset γ_i is set by

$$\gamma_i = \begin{cases} 0 & \text{for } \beta_i \geq 0, \\ \beta_i^2/4\alpha_i & \text{for } \beta_i < 0. \end{cases} \tag{17}$$

The best-fit value of $m_{\beta\beta}$ is set by:

$$\Delta\chi_i^2 = 0 \to m_{\beta\beta} = \begin{cases} 0 & \text{for } \beta_i \geq 0, \\ (-\beta_i/2\alpha_i)^{1/2} & \text{for } \beta_i < 0. \end{cases} \tag{18}$$

Table III reports the parametric coefficients $(\alpha_i, \beta_i, \gamma_i)$ for the Xe, Ge, Te and Te* cases, with their explicit dependence on the matrix elements M_{Xe}, M_{Ge}, M_{Te}.

Constraints on $m_{\beta\beta}$ from two or more isotopes are obtained by summing the corresponding $\Delta\chi_i^2$, and by adjusting the offset so that it obeys Eq. (17), namely: $\Delta\chi^2 = \alpha m_{\beta\beta}^4 + \beta m_{\beta\beta}^2 + \gamma$, where $\alpha = \sum_i \alpha_i$, $\beta = \sum_i \beta_i$, and $\gamma = 0$ for $\beta \geq 0$ ($\gamma = \beta^2/4\alpha$ otherwise). Bounds on $m_{\beta\beta}$ at a given confidence level are obtained by solving

$$\Delta\chi^2(m_{\beta\beta}) = \Delta_{\mathrm{CL}}, \tag{19}$$

where, e.g., $\Delta_{\mathrm{CL}} = 2.706$, 4 and 9 for limits at 90% C.L., 2σ and 3σ, respectively.

Two qualitatively different cases arise from current results: (a) for Xe, Ge and Te*, either separately or in combination, there is no offset γ and the $\Delta\chi^2$ function is zeroed at $m_{\beta\beta} = 0$; (b) for Te results, characterized by $\gamma_i > 0$ (positive fluctuation), the combination with Xe or Ge (or both) may lead to $\gamma > 0$, implying a nonzero Majorana neutrino mass at best fit: $m_{\beta\beta} = [-\beta/2\alpha]^{1/2}$. We discuss separately these two cases below.

A. Combination of Xe, Ge, Te* constraints

In this section we consider current constraints from Xe, Ge, and from the pseudoexperiment Te* (corresponding to null signal in CUORE). In this case the analysis is straightforward, since the best fit is $m_{\beta\beta} = 0$ for all isotopes and their combinations (independently of the NME). The analysis including real Te data will bring forward cases with $m_{\beta\beta} > 0$ at best fit, as discussed in the next section.

We consider both separate and combined Xe, Ge and Te* constraints, as obtained by summing up the corresponding

TABLE III. Coefficients of the quadratic parametrization $\Delta\chi_i^2 = \alpha_i m_{\beta\beta}^4 + \beta_i m_{\beta\beta}^2 + \gamma_i$ for the cases Xe, Ge, Te and Te*.

Case	α_i	β_i	γ_i
Xe	$1.223 \times 10^{-9} M_{\mathrm{Xe}}^4$	$5.380 \times 10^{-5} M_{\mathrm{Xe}}^2$	0
Ge	0	$1.344 \times 10^{-5} M_{\mathrm{Ge}}^2$	0
Te	$5.094 \times 10^{-11} M_{\mathrm{Te}}^4$	$-9.186 \times 10^{-6} M_{\mathrm{Te}}^2$	0.414
Te*	$5.094 \times 10^{-11} M_{\mathrm{Te}}^4$	0	0

TABLE IV. Bounds on $m_{\beta\beta}$/meV at 2σ level from Xe, Ge and Te* results, both separately and in combination, for each of the 15 representative NME calculations listed in Table II. The best-fit value is $m_{\beta\beta} = 0$ in all cases.

	1	2	3	4	5	6	7	8	9	10	11	12	13	14	15
Xe	86.9	80.9	121.6	112.6	82.9	127.9	68.1	72.9	178.6	168.0	47.2	41.6	46.7	61.0	58.3
Ge	188.8	177.7	161.9	152.8	205.1	107.2	103.7	112.5	174.9	160.5	118.6	98.3	90.3	106.2	86.1
Te*	191.8	178.8	295.7	274.3	167.5	386.4	132.3	113.4	182.5	164.4	103.2	82.6	108.3	133.7	127.6
Xe + Ge	81.0	75.5	101.9	95.0	78.5	86.8	59.3	63.7	132.0	122.7	44.8	39.2	42.8	54.8	50.4
Xe + Te*	85.7	79.8	120.4	111.6	81.3	127.4	66.6	69.2	147.2	135.3	46.5	40.7	46.2	60.1	57.5
Ge + Te*	149.7	140.2	155.6	146.5	142.2	106.9	91.3	88.8	140.7	127.8	85.8	69.5	77.5	92.9	79.4
Xe + Ge + Te*	80.1	74.7	101.3	94.4	77.2	86.7	58.4	61.5	120.4	110.7	44.2	38.5	42.4	54.2	49.9

functions defined in Table III, $\Delta\chi^2 = \sum_i \Delta\chi_i^2 = \alpha m_{\beta\beta}^4 + \beta m_{\beta\beta}^2$. For a given choice of M_i, upper limits on $m_{\beta\beta}$ are obtained by solving $\Delta_{\rm CL} = \alpha m_{\beta\beta}^4 + \beta m_{\beta\beta}^2$. For definiteness we set $\Delta_{\rm CL} = 4$ (2σ bounds), unless otherwise specified.

Table IV reports the upper bounds on $m_{\beta\beta}$, for each of the representative ($M_{\rm Xe}$, $M_{\rm Ge}$, $M_{\rm Te}$) calculations listed in Table II. Concerning constraints from single isotopes, in most cases Xe sets the strongest bound, followed by weaker ones from Ge and Te*. However, for the cases numbered as 9 and 10 (QRPA), the bounds from Xe, Ge and Te* are comparable to each other, and for case 6 (QRPA) the Ge bound actually prevails over the Xe (and Te*) bound. Notice that such a hierarchy of $m_{\beta\beta}$ constraints may change at different confidence levels, since the S_i bounds scale up at different rates (see Fig. 2). In Table IV the combination of pairs of constraints improves appreciably upon each separate constraint; the relative balance in each pair is highlighted below. Finally, the total combination Xe + Ge + Te* provides even stronger bounds on $m_{\beta\beta}$, that range from a minimum of 38.5 meV (case 12, EDF) to a maximum of 120.4 meV (case 9, QRPA) at 2σ.

Figure 4 shows isolines of the 2σ bounds on $m_{\beta\beta}$, as derived by combining any two pairs among Xe, Ge and Te*, for unconstrained values of the NME. In each panel, single-isotope bounds are asymptotically recovered along each axis, for vanishing matrix element on the other axis. When both matrix elements are sizeable, the joint bound improves upon separate ones. In particular, at each marked point, the bounds in Table IV are recovered for the corresponding NME and pair of isotopes.

For each (M_x, M_y) panel and (x, y) isotope pair, the condition for the dominance of one isotope constraint over the other is easily derived. The two isotopes contribute equally to $\Delta_{\rm CL}$ when $\Delta\chi_x^2 = \Delta_{\rm CL}/2 = \Delta\chi_y^2$. The solutions to these equations read $M_x m_{\beta\beta} = \xi_x$ and $M_y m_{\beta\beta} = \xi_y$, where $\xi_{x,y}$ are positive numbers. For $\Delta_{\rm CL}=4$ it is $M_{\rm Te}/M_{\rm Ge} = 1.154$, $M_{\rm Ge}/M_{\rm Xe} = 2.488$, and $M_{\rm Te}/M_{\rm Xe} = 2.871$, shown as a dashed line in each panel of Fig. 4. Along the dashed line, the two isotopes contribute with equal strength to the 2σ upper bound; above the dashed line, the y-axis isotope dominates over the x-axis one, and vice versa. In this way one gets a graphical interpretation of the hierarchy of bounds for different NME, that was inferred from numerical inspection of Table IV.

B. Combination of Xe, Ge, Te constraints

In this section we consider real Te data, as opposed to the previous cases including Te* pseudodata. The slight preference of Te data from CUORE for a nonzero signal (as compared with Xe, Ge and Te*, see Fig. 2) brings forward new features of multi-isotope data constraints, although still at embryonic stages.

In general one may expect that, for relatively small values of $M_{\rm Te}$ (with respect to $M_{\rm Xe}$ and $M_{\rm Ge}$), the Xe + Ge results will dominate over Te, keeping the best fit at

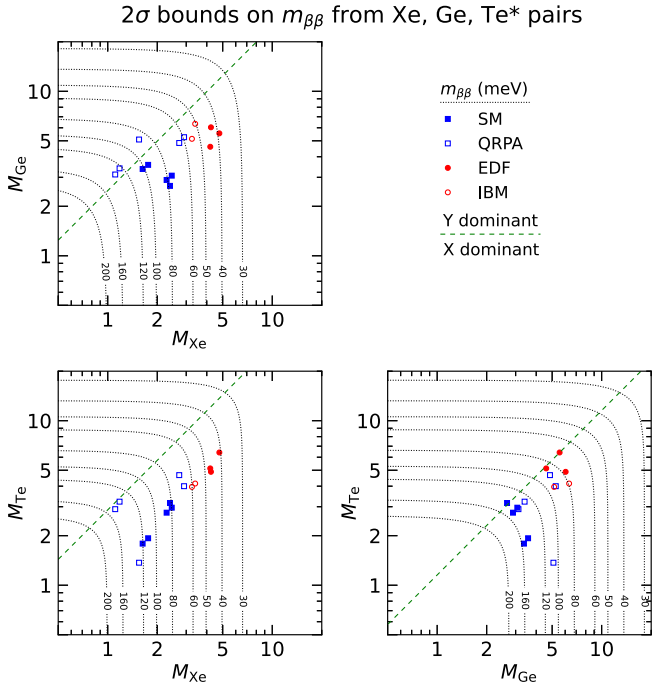

FIG. 4. Isolines of $m_{\beta\beta}$ bounds (at 2σ level) in the landscape of nuclear matrix elements, obtained from the combination of any two results among Xe, Ge and Te*. In each panel, the bounds are dominated by the isotope on the y (x) axis, in the region above (below) the dashed line. See the text for details.

TABLE V. Upper half: Bounds on $m_{\beta\beta}/\mathrm{meV}$ at 2σ level from Xe, Ge and Te results, both separately and in combination, for each of the 15 representative NME calculations listed in Table II. Lower half: Corresponding best-fit values of $m_{\beta\beta}$.

	1	2	3	4	5	6	7	8	9	10	11	12	13	14	15
Xe	86.9	80.9	121.6	112.6	82.9	127.9	68.1	72.9	178.6	168.0	47.2	41.6	46.7	61.0	58.3
Ge	188.8	177.7	161.9	152.8	205.1	107.2	103.7	112.5	174.9	160.5	118.6	98.3	90.3	106.2	86.1
Te	220.5	205.6	340.0	315.3	192.6	444.2	152.1	130.3	209.9	189.0	118.6	94.9	124.5	153.7	146.6
Xe + Ge	81.0	75.5	101.9	95.0	78.5	86.8	59.3	63.7	132.0	122.7	44.8	39.2	42.8	54.8	50.4
Xe + Te	89.6	83.4	124.9	115.7	85.6	130.4	70.4	75.0	167.5	154.5	48.6	42.9	48.1	62.9	60.1
Ge + Te	174.1	163.2	170.1	160.5	166.5	109.6	104.4	103.3	163.4	148.6	100.3	81.3	89.2	106.5	89.2
Xe + Ge + Te	83.5	77.9	104.5	97.4	81.2	88.0	61.4	66.2	135.0	124.7	46.2	40.5	44.1	56.5	51.9
Xe	0	0	0	0	0	0	0	0	0	0	0	0	0	0	0
Ge	0	0	0	0	0	0	0	0	0	0	0	0	0	0	0
Te	108.8	101.4	167.7	155.6	95.0	219.2	75.1	64.3	103.5	93.2	58.5	46.8	61.4	75.8	72.4
Xe + Ge	0	0	0	0	0	0	0	0	0	0	0	0	0	0	0
Xe + Te	0	0	0	0	0	0	0	0	31.7	36.0	0	0	0	0	0
Ge + Te	0	0	0	0	0	0	0	0	0	0	0	0	0	0	0
Xe + Ge + Te	0	0	0	0	0	0	0	0	0	0	0	0	0	0	0

$m_{\beta\beta} = 0$. However, for increasing M_{Te}, the Te results will eventually prevail and set $m_{\beta\beta} > 0$ at $\Delta\chi^2 = 0$, affecting also upper bounds at some value Δ_{CL}.

This situation anticipates what could happen with future and more accurate $0\nu\beta\beta$ data: their combination may (or may not) be consistent with some indications for nonzero $m_{\beta\beta}$, depending on both the data and the NME values. A future preference for $m_{\beta\beta} > 0$ might even lead to lower bounds on $m_{\beta\beta}$, either separately or in combination, depending in part on (un)favorable values of the NME. Eventually, precise multi-isotope data might even test specific NME's by selecting allowed ratios M_x/M_y [29,30] namely, slanted allowed stripes in the NME landscape of Fig. 3.[3]

In our approach, the occurrence of $m_{\beta\beta} > 0$ at best fit is simply signaled, for a single isotope, by a coefficient $\beta_i < 0$ in the $\Delta\chi^2$ function (currently occurring only for Te) and, for any combination of multi-isotope data, by a negative coefficient $\beta = \sum_i \beta_i < 0$. The best-fit value of $m_{\beta\beta}$ is then $m_{\beta\beta} = (-\beta/2\alpha)^{1/2}$ with $\alpha = \sum_i \alpha_i$, and its specific value depends on the NME's. For $\beta < 0$, the offset must be taken as $\gamma = \beta^2/4\alpha$. In all cases, upper bounds at a chosen confidence levels are set by $\Delta\chi^2 = \Delta_{\mathrm{CL}}$. Table V shows the numerical results from current Xe, Ge and Te data, regarding the 2σ limits (lower part) and the best-fit values (lower half) of $m_{\beta\beta}$. In the upper half, the rows corresponding the Xe, Ge and Ge + Xe are unchanged with respect to Table IV, but are repeated for completeness.

Let us first comment on the $m_{\beta\beta}$ best fits in the lower half of Table V. Of course, the Te row displays nonzero results, with $m_{\beta\beta}$ scaling as $1/M_{\mathrm{Te}}$. In almost all cases including Te (combined with Xe or Ge or both), the positive contributions to $\beta = \sum_i \beta_i$ from $i = \mathrm{Xe}$ and Ge are never erased by the negative contribution from Te, and $m_{\beta\beta} = 0$ is preferred. Only for cases 9 and 10 (QRPA), it turns out that the large ratio $M_{\mathrm{Te}} \simeq 2.6 M_{\mathrm{Xe}}$ makes Te prevail over Xe in the corresponding Xe + Te combinations, which show nonzero best fits.

Concerning the upper half of Table V, the combination of Te with Xe (or Ge) does not necessarily improve upon the separate 2σ bounds. Roughly speaking, when the best-fit value of $m_{\beta\beta}$ in Te is comparable or larger than the upper bound from Xe (Ge) alone, the joint bound from Xe + Te (Ge + Te) is weakened, as a result of the slight tension between the two isotopic data. A slight weakening also occurs whenever when Te is added to Xe + Ge in the global combination Xe + Ge + Te.[4] The 2σ bounds on $m_{\beta\beta}$ compiled in Table V are contained in the following range:

$$m_{\beta\beta} \in [40.5, 135.0]\ \mathrm{meV}\ (\mathrm{Xe} + \mathrm{Ge} + \mathrm{Te}). \quad (20)$$

The lowest (most optimistic) edge of this range would significantly cut from above the IO and NO allowed regions in Fig. 1, setting also an upper limit on Σ at the level of ∼400 meV.

Figure 5 shows isolines of the best-fit value of $m_{\beta\beta}$ in the left and right panels charted by (Xe, Te) and (Ge, Te), respectively. In the left panel, the condition $\sum_i \beta_i > 0$ for $m_{\beta\beta} > 0$ implies $M_{\mathrm{Te}}/M_{\mathrm{Xe}} > 2.42$, satisfied only by two marked points (corresponding to the QRPA cases 9 and 10 in Table II) close to the isoline at $m_{\beta\beta} = 30$ meV. In the right panel, none of the marked points falls in the analogous

[3]An overall NME rescaling factor λ ($M_{x,y} \to \lambda M_{x,y}$) is degenerate with an inverse rescaling of the Majorana mass ($m_{\beta\beta} \to m_{\beta\beta}/\lambda$).

[4]These effects are analogous to those noted in Sec. II B for the combination of KamLAND-Zen and EXO data, leading to a T_{90} bound slightly weaker than from KamLAND-Zen alone, as a result of two opposite fluctuations.

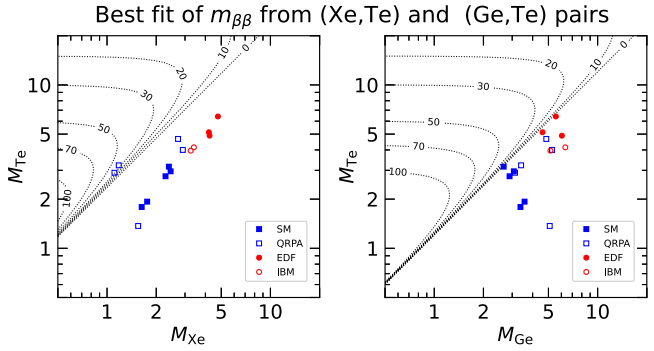

FIG. 5. Isolines of best-fit values of $m_{\beta\beta}$/meV in the planes charted by (Xe, Te) and (Ge, Te) nuclear matrix elements. The best fit is zero in the lower-right parts of each panel, as well as in the whole (Xe, Ge) panel (not shown).

region $M_{Te}/M_{Ge} > 1.21$, although three of them are very close to its border. If future $0\nu\beta\beta$ experiments will show some indications for a signal, plots like these will help to locate the best-fit values of $m_{\beta\beta}$ as a function of the NME, for each isotope pair. The (in)consistency of the best fits in different pairs will provide interesting clues about the interpretation of data in terms of light Majorana neutrinos.

Figure 6 shows isolines of the $m_{\beta\beta}$ upper bounds at 2σ, in the same planes of Fig. 5. In comparison with the lower panels of Fig. 4, a slight weakening of the bounds can be appreciated. Note that, in the presence of subregions where $m_{\beta\beta} > 0$ at best fit, the offset γ depends on information coming from both isotopes, whose χ^2 contributions cannot be separated in the combination. The condition of equal contributions to Δ_{CL} cannot be defined in general terms, and the dashed lines of Fig. 4 are thus absent in Fig. 6.

We conclude this section by discussing the constraints on $m_{\beta\beta}$ at various confidence levels, as derived from the global combination of current (Xe + Ge + Te) data, using the representative NME values in Table II. Since the best fit is $m_{\beta\beta} = 0$ in all Xe + Ge + Te cases (see Table V), only upper bounds need to be quoted.

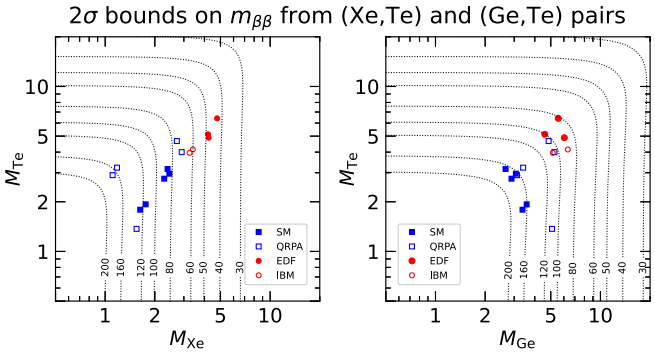

FIG. 6. Isolines of $m_{\beta\beta}$ bounds (at 2σ level) in the planes charted by (Xe, Te) and (Ge, Te) nuclear matrix elements. The (Xe, Ge) panel (not shown) is unchanged with respect to Fig. 4.

TABLE VI. Upper bounds on $m_{\beta\beta}$/meV at 90% C.L., 2σ, and 3σ, from the combination of current Xe + Ge + Te data, for the representative NME calculations considered in this work.

	90%	2σ	3σ	Model
1	72.7	83.5	109.4	
2	67.8	77.9	101.9	
3	89.3	104.5	141.5	SM
4	83.3	97.4	131.7	
5	71.0	81.2	105.4	
6	73.6	88.0	125.3	
7	53.0	61.4	81.6	
8	57.6	66.2	86.7	QRPA
9	117.7	135.0	176.3	
10	108.9	124.7	162.3	
11	40.3	46.2	60.1	
12	35.4	40.5	52.6	EDF
13	38.2	44.1	58.1	
14	48.8	56.5	74.7	
15	44.6	51.9	69.5	IBM

Table VI reports the 90% C.L., 2σ, and 3σ upper limits on $m_{\beta\beta}$ (in meV). Figure 7 shows the $N_\sigma = (\Delta\chi^2)^{1/2}$ bounds as continuous functions of $m_{\beta\beta}$. Qualitatively, the strongest limits in are obtained using NMEs from the EDF and IBM models, followed by QRPA and SM cases in mixed order. These results can be generalized to any other choice of NME calculations, using the information provided in this paper.

In Fig. 7, one of the N_σ curves labeled as QRPA shows a a markedly different (almost linear) slope, intersecting three SM curves. This peculiar curve corresponds to the lowest QRPA point in both panels of Fig. 6 (case 6 in Table II), that is characterized by a rather large value of M_{Ge} as compared with $M_{Xe,Te}$. As a result, Ge data prevail over Xe and Te in the combination, and the leading dependence is $\Delta\chi^2 \propto S \propto m_{\beta\beta}^2$ (rather than $\Delta\chi^2 \propto S^2 \propto m_{\beta\beta}^4$), implying a roughly

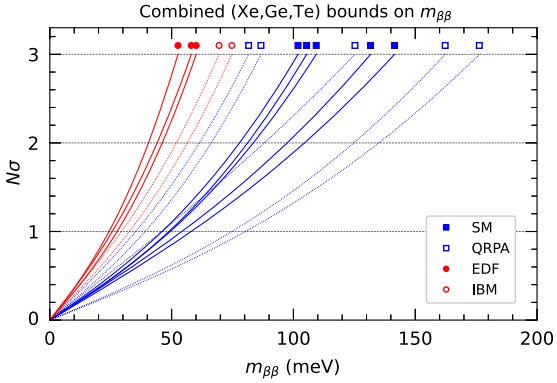

FIG. 7. Significance of upper limits on $m_{\beta\beta}$ in terms of $N_\sigma = (\Delta\chi^2)^{1/2}$, from the combination of current Xe + Ge + Te data, for the representative NME calculations considered in this work.

linear $N_\sigma(m_{\beta\beta})$ function. Once more, this observation shows the importance of considering the full likelihood profile of the experimental results (e.g., in terms of $S = 1/T$), rather than pointlike information (such as the 90% C.L. limit on T).

As a final step, one could include a joint probability distribution or a $\Delta\chi^2$ penalty defined over the NME landscape $(M_{\rm Xe}, M_{\rm Ge}, M_{\rm Te})$, and numerically minimize the total $\Delta\chi^2$ function. This exercise was performed in [3] by assuming a conservative characterization of the NME and their correlated uncertainties, derived within QRPA calculations [27]. A limit $m_{\beta\beta} < 110$ meV was obtained at 2σ [3]. By repeating the same exercise with the updated (Xe + Ge + Te) combination considered herein, we get the following marginalized bounds (in meV): $m_{\beta\beta} < 79.5$ at 90% C.L., $m_{\beta\beta} < 99.8$ at 2σ, and $m_{\beta\beta} < 169$ at 3σ. Roughly speaking, from these results and from the summary in Eq. (20) one can state that the combination of current $0\nu\beta\beta$ experiments sets 2σ upper bounds on $m_{\beta\beta}$ at the level of ∼90–100 meV for "average" NME values, possibly lowered to ∼40–50 meV for favorable NME values.

A final remark is in order. In principle, one should replace the QRPA input from [27] with more general and up-to-date estimates of the NME's and their uncertainties, characterizing also the spread among different models and calculations. However, no consensus estimates exist yet for NME fiducial values and covariances, although relevant work is in progress toward this goal [1,31]. Part of the planned strategy involves benchmarking nuclear models for $0\nu\beta\beta$ decay against a variety of data, coming from related electroweak and strong interaction processes or from nuclear structure [32–35].

IV. CONCLUSIONS AND PERSPECTIVES

We have discussed an approach to the analysis of neutrinoless double beta decay experiments, in terms of $\Delta\chi^2$ profiles for the signal strength S_i (inverse of the half-life T_i) in the isotopes i = Xe, Ge and Te, building upon previous work [3]. The approach becomes exceedingly simple for quadratic approximations to such profiles, implying quadratic (in)equalities in the landscape of nuclear matrix elements M_i that connect the S_i to the Majorana mass $m_{\beta\beta}$. For convenience, some results have been discussed in terms of pseudo data for null signal in Te (dubbed Te*). Simple relations among the M_i have been derived to gauge the relative contributions of different isotopic data in setting upper limits to $m_{\beta\beta}$ (for null best fits in Xe, Ge and Te*), and to identify the conditions leading to a preference for nonzero $m_{\beta\beta}$ (for generic Xe, Ge and Te data). Using the latest available $0\nu\beta\beta$ data, as well as representative values of the NME from different models, we have discussed current constraints on $m_{\beta\beta}$ at several confidence levels and in various combinations, both numerically and graphically. Global 2σ upper limits on $m_{\beta\beta}$ are found in the range from 40.5 to 135 meV, depending on the NME.

The approach can be easily extended to nonstandard processes for $0\nu\beta\beta$ decay [1,36,37] by replacing the relation $S_i = G_i M_i^2 m_{\beta\beta}^2$ with the appropriate phase space, NME and particle physics parameter characterizing the process. Also, the approach can be extended to generic $\Delta\chi^2(S_i)$ functions, with a modest price to pay in terms of numerical (rather than analytical) solutions. We invite the experimental collaborations involved in $0\nu\beta\beta$ decay searches to publicly provide such $\Delta\chi^2(S_i)$ functions or equivalent ones, as they contain much more information than the usually quoted 90% C.L. limits on T_i. Indeed, the relative impact of such limits and of the resulting bounds on $m_{\beta\beta}$ in a multi-isotope combination depend sensitively on the likelihood profiles of S_i (or T_i), and not only on the relative size of the M_i.

Our approach to the multi-isotope data analysis would be complete if one could also assign joint probability densities to the M_i, whose variations could then be treated as nuisance parameters and marginalized. So far, detailed results for the NME central values and covariances, including g_A quenching uncertainties, have been obtained in a specific (QRPA) model [27]. In perspective, it would be important to extend such investigations to other nuclear models, eventually reaching consensus values for the M_i and for their correlated (and possibly reduced) uncertainties.

In this sense, the combined analysis of $0\nu\beta\beta$ results is proceeding through to the same steps that have characterized similar fields (e.g., solar neutrinos) in the past: from low-statistics data and theoretical models with large uncertainties, to a wealth of accurate experimental results interpreted in increasingly refined and constrained models. Our work aims at providing one methodological step along this path.

ACKNOWLEDGMENTS

This work is partly supported by the Italian Ministero dell'Università e Ricerca (MUR) through the research Grant No. 2017W4HA7S "NAT-NET: Neutrino and Astroparticle Theory Network" under the program PRIN 2017, and by the Istituto Nazionale di Fisica Nucleare (INFN) through the "Theoretical Astroparticle Physics" (TAsP) project. We thank K. Inoue for useful information about the latest KamLAND-Zen data release [14].

[1] M. Agostini, G. Benato, J. A. Detwiler, J. Menéndez, and F. Vissani, Toward the discovery of matter creation with neutrinoless double-beta decay, arXiv:2202.01787.

[2] P. A. Zyla *et al.* (Particle Data Group Collaboration), Review of particle physics, Prog. Theor. Exp. Phys. **2020**, 083C01 (2020).

[3] F. Capozzi, E. Di Valentino, E. Lisi, A. Marrone, A. Melchiorri, and A. Palazzo, Unfinished fabric of the three neutrino paradigm, Phys. Rev. D **104**, 083031 (2021).

[4] K. N. Abazajian *et al.*, Synergy between cosmological and laboratory searches in neutrino physics: A white paper, arXiv:2203.07377.

[5] S. Abe *et al.* (KamLAND-Zen Collaboration), First search for the Majorana nature of neutrinos in the inverted mass ordering region with KamLAND-Zen, arXiv:2203.02139.

[6] G. Anton *et al.* (EXO-200 Collaboration), Search for Neutrinoless Double-β Decay with the Complete EXO-200 Dataset, Phys. Rev. Lett. **123**, 161802 (2019).

[7] M. Agostini *et al.* (GERDA Collaboration), Final Results of GERDA on the Search for Neutrinoless Double-β Decay, Phys. Rev. Lett. **125**, 252502 (2020).

[8] S. I. Alvis *et al.* (MAJORANA Collaboration), A search for neutrinoless double-beta decay in ^{76}Ge with 26 kg-yr of exposure from the MAJORANA DEMONSTRATOR, Phys. Rev. C **100**, 025501 (2019).

[9] D. Q. Adams *et al.* (CUORE Collaboration), Search for Majorana neutrinos exploiting millikelvin cryogenics with CUORE, Nature (London) **604**, 53 (2022); See also: High sensitivity neutrinoless double-beta decay search with one tonne-year of CUORE data, arXiv:2104.06906.

[10] A. Caldwell, A. Merle, O. Schulz, and M. Totzauer, Global Bayesian analysis of neutrino mass data, Phys. Rev. D **96**, 073001 (2017).

[11] S. D. Biller, Combined constraints on Majorana masses from neutrinoless double beta decay experiments, Phys. Rev. D **104**, 012002 (2021).

[12] B. Märkisch, H. Mest, H. Saul, X. Wang, H. Abele, D. Dubbers, M. Klopf, A. Petoukhov, C. Roick, T. Soldner, and D. Werder, Measurement of the Weak Axial-Vector Coupling Constant in the Decay of Free Neutrons Using a Pulsed Cold Neutron Beam, Phys. Rev. Lett. **122**, 242501 (2019).

[13] J. T. Suhonen, Value of the axial-vector coupling strength in β and $\beta\beta$ decays: A review, Front. Phys. **5**, 55 (2017).

[14] K. Inoue (private communication). We thank the KamLAND Collaboration for sharing the digitized likelihood function used in [5].

[15] J. Menéndez, Neutrinoless $\beta\beta$ decay mediated by the exchange of light and heavy neutrinos: The role of nuclear structure correlations, J. Phys. G **45**, 014003 (2018).

[16] M. Horoi and A. Neacsu, Shell model predictions for ^{124}Sn double-β decay, Phys. Rev. C **93**, 024308 (2016).

[17] L. Coraggio, A. Gargano, N. Itaco, R. Mancino, and F. Nowacki, Calculation of the neutrinoless double-β decay matrix element within the realistic shell model, Phys. Rev. C **101**, 044315 (2020).

[18] M. T. Mustonen and J. Engel, Large-scale calculations of the double-β decay of ^{76}Ge, ^{130}Te, ^{136}Xe, and ^{150}Nd in the deformed self-consistent Skyrme quasiparticle random-phase approximation, Phys. Rev. C **87**, 064302 (2013).

[19] J. Hyvärinen and J. Suhonen, Nuclear matrix elements for $0\nu\beta\beta$ decays with light or heavy Majorana-neutrino exchange, Phys. Rev. C **91**, 024613 (2015).

[20] F. Šimkovic, A. Smetana, and P. Vogel, $0\nu\beta\beta$ nuclear matrix elements, neutrino potentials and SU(4) symmetry, Phys. Rev. C **98**, 064325 (2018).

[21] D. L. Fang, A. Faessler, and F. Simkovic, $0\nu\beta\beta$ -decay nuclear matrix element for light and heavy neutrino mass mechanisms from deformed quasiparticle random-phase approximation calculations for ^{76}Ge, ^{82}Se, ^{130}Te, ^{136}Xe, and ^{150}Nd with isospin restoration, Phys. Rev. C **97**, 045503 (2018).

[22] T. R. Rodriguez and G. Martinez-Pinedo, Energy Density Functional Study of Nuclear Matrix Elements for Neutrinoless $\beta\beta$ Decay, Phys. Rev. Lett. **105**, 252503 (2010).

[23] N. López Vaquero, T. R. Rodríguez, and J. L. Egido, Shape and Pairing Fluctuations Effects on Neutrinoless Double Beta Decay Nuclear Matrix Elements, Phys. Rev. Lett. **111**, 142501 (2013).

[24] L. S. Song, J. M. Yao, P. Ring, and J. Meng, Nuclear matrix element of neutrinoless double-β decay: Relativity and short-range correlations, Phys. Rev. C **95**, 024305 (2017).

[25] J. Barea, J. Kotila, and F. Iachello, $0\nu\beta\beta$ and $2\nu\beta\beta$ nuclear matrix elements in the interacting boson model with isospin restoration, Phys. Rev. C **91**, 034304 (2015).

[26] F. F. Deppisch, L. Graf, F. Iachello, and J. Kotila, Analysis of light neutrino exchange and short-range mechanisms in $0\nu\beta\beta$ decay, Phys. Rev. D **102**, 095016 (2020).

[27] A. Faessler, G. L. Fogli, E. Lisi, V. Rodin, A. M. Rotunno, and F. Simkovic, QRPA uncertainties and their correlations in the analysis of $0\nu\beta\beta$ decay, Phys. Rev. D **79**, 053001 (2009).

[28] S. Stoica and M. Mirea, Phase space factors for double-beta decays, Front. Phys. **7**, 12 (2019).

[29] S. M. Bilenky and J. A. Grifols, The possible test of the calculations of nuclear matrix elements of the $(\beta\beta)_{0\nu}$ decay, Phys. Lett. B **550**, 154 (2002).

[30] S. M. Bilenky and S. T. Petcov, Nuclear matrix elements of $0\nu\beta\beta$ decay: Possible test of the calculations, arXiv:hep-ph/0405237.

[31] J. Engel and J. Menéndez, Status and future of nuclear matrix elements for neutrinoless double-beta decay: A review, Rep. Prog. Phys. **80**, 046301 (2017).

[32] H. Ejiri, J. Suhonen, and K. Zuber, Neutrino–nuclear responses for astro-neutrinos, single beta decays and double beta decays, Phys. Rep. **797**, 1 (2019).

[33] V. Cirigliano, Z. Davoudi, W. Dekens, J. de Vries, J. Engel, X. Feng, J. Gehrlein, M. L. Graesser, L. Gráf, H. Hergert, L. Jin, E. Mereghetti, A. Nicholson, S. Pastore, M. J. Ramsey-Musolf, R. Ruiz, M. Spinrath, U. van Kolck, and André Walker-Loud, Neutrinoless double-beta decay: A roadmap for matching theory to experiment, arXiv:2203.12169.

[34] M. Horoi, A. Neacsu, and S. Stoica, A statistical analysis for the neutrinoless double-beta decay matrix element of ^{48}Ca, arXiv:2203.10577.

[35] H. Ejiri, L. Jokiniemi, and J. Suhonen, Nuclear matrix elements for neutrinoless $\beta\beta$ decays and spin-dipole giant resonances, Phys. Rev. C **105**, L022501 (2022).

[36] M. J. Dolinski, A. W. P. Poon, and W. Rodejohann, Neutrinoless double-beta decay: Status and prospects, Annu. Rev. Nucl. Part. Sci. **69**, 219 (2019).

[37] W. Rodejohann, Neutrino-less double beta decay and particle physics, Int. J. Mod. Phys. E **20**, 1833 (2011).